

Which Oxidation State Leads to O–O Bond Formation in Cp*Ir(bpy)Cl-Catalyzed Water Oxidation, Ir(V), Ir(VI), or Ir(VII)?

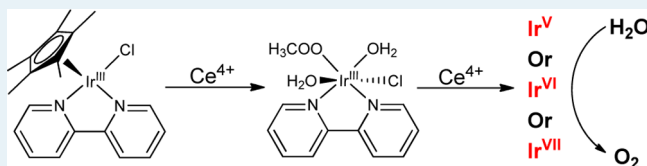
Rong-Zhen Liao* and Per E. M. Siegbahn*

Department of Organic Chemistry, Arrhenius Laboratory, Stockholm University, SE-10691 Stockholm, Sweden

S Supporting Information

ABSTRACT: Density functional calculations are used to revisit the reaction mechanism of water oxidation catalyzed by the Cp*Ir(bpy)Cl (Cp* = pentamethylcyclopentadienyl, bpy = 2,2'-bipyridine) complex. One of the experimentally suggested active species [(bpy)Ir(H₂O)₂(HCOO)Cl]⁺ can undergo very facile intramolecular formate oxidation at higher oxidation state even though it can also promote O–O bond formation. Therefore, [(bpy)Ir(H₂O)₂(CH₃COO)Cl]⁺ is here proposed to be the most likely precatalyst as acetate was also experimentally observed after Cp* oxidation. O–O bond formation takes place at the high formal oxidation states of Ir^{VI} and Ir^{VII}, rather than that of Ir^V, as suggested before. Three sequential proton-coupled electron transfer oxidations result in the formation of a highly oxidized intermediate, [(bpy)Ir^{VI}O(OH)(CH₃COO)Cl]⁺. From this formal Ir^{VI} intermediate, O–O bond formation takes place by a water attack on the Ir^{VI}=O moiety assisted by the acetate ligand, which abstracts a proton during the attack. The barrier was calculated to be very facile, being 14.7 kcal/mol, in good agreement with experimental kinetic results, which gave a barrier of around 18 kcal/mol. The attack leads to the formation of an Ir^{IV}-peroxide intermediate, which undergoes proton-coupled electron transfer to form an Ir^{III}–O₂ intermediate. Finally, O₂ can be released, coupled with the binding of another water molecule, to regenerate the catalytic Ir^{III} species. Water oxidation at Ir^{VII} has a slightly higher barrier, but it may also contribute to the activity. However, water oxidation at Ir^V has a significantly higher barrier. Acetate oxidation by C–H activation was found to have a much higher barrier, suggesting that [(bpy)Ir(H₂O)₂(CH₃COO)Cl]⁺ is a remarkably stable catalyst. The possible catalytic species [(bpy-dc)Ir^{III}(H₂O)₃Cl]²⁺ without acetate coordination has also been considered and also gave a reasonably feasible barrier for the water oxidation. O–O bond formation at Ir^{VII} is slightly preferred compared with at Ir^{VI}, which is different from the case with acetate.

KEYWORDS: water oxidation, reaction mechanism, density functional calculations, iridium, proton-coupled electron transfer

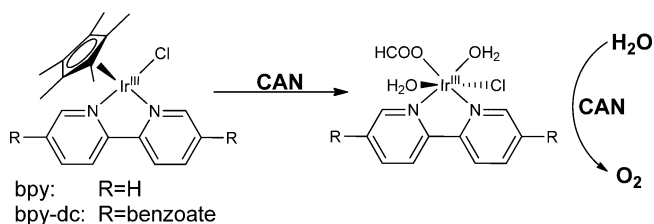


1. INTRODUCTION

Water splitting, coupled with the production of clean fuels, such as H₂, is one of the most encouraging methods of solar energy harnessing and storage.^{1,2} The oxidation of water by releasing four protons and four electrons is thermodynamically unfavorable with a relatively large energy demand ($E_0 = 1.23$ V vs SHE at pH = 0) and is therefore quite challenging to accomplish. During the last few decades, considerable progress has been achieved in the development of homogeneous water oxidation catalysts (WOCs) using transition metals, such as ruthenium,^{3,4} iridium,^{5,6} vanadium,⁷ manganese,^{8,9} iron,^{10,11} cobalt,^{12,13} and copper.^{14,15}

Crabtree, Brudvig, and co-workers have reported a series of half-sandwich Cp*Ir(III) complexes (Cp* = pentamethylcyclopentadienyl) that enable water oxidation using ceric ammonium nitrate (CAN) as the chemical oxidant.^{6,16} Among them, Cp*Ir(bpy)Cl (bpy = 2,2'-bipyridine, Scheme 1) was found to have the highest activity, with an initial turnover frequency of 14.4 min⁻¹ and a turnover number of 155 during the first hour.¹⁶ ¹⁸O labeling of water confirmed that the oxygen evolved comes from water. Kinetic studies showed that oxygen evolution is first-order in the iridium catalyst. In addition, the rate is less than first-order (0.73) in CAN when

Scheme 1. Schematic Representation of Cp*Ir(bpy-dc)Cl and its Oxidative Transformation



the concentration of the oxidant is low, whereas it becomes zero-order in CAN when the concentration of the oxidant is high. The H/D kinetic isotope effect has been measured within two different concentrations of CAN, and an inverse KIE of 0.65 was obtained at 8 mM CAN, although a normal KIE of 1.2 was found at 243 mM CAN. The involvement of IrO₂ nanoparticles has been safely ruled out on the basis of its different H/D kinetic isotope effect. Density functional theory

Received: August 8, 2014

Revised: September 24, 2014

(DFT) calculations have also been performed to elucidate the O–O bond formation mechanism.¹⁶ It was suggested that O–O bond formation takes place by a nucleophilic attack of a water molecule on the Ir^V=O moiety, coupled with proton transfer to the oxo group assisted by a second water molecule. The electronic energy barrier at the B3LYP¹⁷ level (SDD¹⁸ pseudopotential for Ir and 6-31G(d,p) basis sets for other elements) was calculated to be 24.0 kcal/mol, while the free energy barrier was found to be over 30 kcal/mol. Compared to experimental kinetic studies, which suggest a free energy barrier of around 18 kcal/mol, the calculated barrier was thus significantly overestimated. Later, Kazaryan and Baerends¹⁹ found that the electronic energy barrier is more than 30 kcal/mol using the B3LYP method with a very large basis set (def2-TZVPP and def2-QZVPP).²⁰ Benchmark calculations using a truncated small model showed that B3LYP gives barriers in good agreement with the highly accurate ab initio CCSD(T) (coupled cluster theory with single and double excitations and a quasiperturbative treatment of connected triple excitations)²¹ method. The Ir^V=O species has also been proposed to promote O–O bond formation in [Ir(OH₂)(phpy)₂] (phpy = *o*-phenylpyridine) on the basis of DFT calculations.²² In that case, the active species was postulated to be [Ir^V(O)(X)(phpy)₂], in which X has been considered to be a water molecule, a hydroxide, or an oxo group. It was found that the free energy barrier decreases by deprotonation of the aqua ligand, from 32.2 kcal/mol for water to 26.1 kcal/mol for hydroxide and further to 19.0 kcal/mol for oxo. The reason is that upon deprotonation, the hydroxide or oxo group can function as a general base to abstract a proton during the water attack. However, the energetic penalty for the deprotonation, which should increase the total barrier significantly, has not been considered.

Recently, Lin and co-workers reported the design of a stable Zr-based metal–organic framework (MOF) using Cp*Ir(bpy-dc)Cl (bpy-dc = dibenzoate-substituted 2,2'-bipyridine, Scheme 1) as a bridging ligand.²³ The immobilization of the WOC in MOF benefits from the following mechanistic advantages: (a) The catalysts are well-separated from each other, restricting the reaction to be first-order in the catalyst and a cooperative dimer mechanism could be safely ruled out. (b) Ligand degradation by intermolecular reactions can be prevented thus increasing the lifetime of the catalyst. (c) IrO₂ nanoparticles, that might be formed during the water oxidation process, can be easily separated and the remaining MOF can be further characterized and used for additional catalytic runs. After the addition of 30 equiv of CAN, acetic acid and formic acid were detected, reconfirming Cp* ligand degradation, as first suggested by Grotjahn and co-workers.²⁴ Electrospray ionization/mass spectrometric analysis of the digested sample suggested that the most likely precatalyst is [(bpy-dc)Ir(H₂O)₂(HCOO)Cl]⁺.²³ However, the coordination of acetate rather than formate to the metal is also possible. The TOF was measured to be 0.48 min⁻¹ by detecting O₂ formation, which corresponds to a barrier of about 20 kcal/mol.

In the present study, the reaction mechanism of this Ir-catalyzed water oxidation is reinvestigated by density functional calculations on the basis of the newly proposed precatalyst. [(bpy)Ir^{III}(H₂O)₂(HCOO)Cl]⁺ cannot account for the observed catalytic activity as formate can be oxidized to generate carbon dioxide. Instead, [(bpy)Ir^{III}(H₂O)₂(CH₃COO)Cl]⁺ is the most likely precatalyst as acetate was also detected after Cp* oxidation, and water oxidation is preferred compared with

acetate oxidation. O–O bond formation initiated by Ir^V=O was found to have a too high barrier that fails to explain the catalytic activity. Instead, O–O bond formation is suggested to take place at a formal Ir^{VI}=O stage with a quite feasible barrier. The use of [(bpy)Ir^{III}(H₂O)₃Cl]²⁺ has also been considered and compared.

2. COMPUTATIONAL DETAILS

The calculations presented were done with the density functional B3LYP,¹⁷ as implemented in the Gaussian 09 program.²⁵ Geometries were optimized using the 6-31G(d,p) basis sets on all elements except for Ir, which were described by the SDD¹⁸ pseudopotential and its corresponding basis sets. The final and the solvation energies were calculated as single-point corrections on the optimized structures using the SMD²⁶ continuum solvation model employing a larger def2-TZVPPD²⁰ basis set (including the SDD pseudopotential for Ir) at the B3LYP*²⁷ (15% exact exchange) level. It has been shown that B3LYP* gives better results in describing relative energies in transition metal complexes.²⁷ D3 dispersion corrections proposed by Grimme²⁸ were also added at single-points. Single-point calculations using other functionals, including B3LYP-D3, M06-D3,²⁹ M06L-D3,³⁰ and PBE1PBE-D3,³¹ have also been carried out to evaluate the sensitivity of redox potentials and barriers with respect to different functionals (vide infra). For water, the experimental solvation free energy of –6.3 kcal/mol is used.³² Analytic frequency calculations were performed on all the optimized structures at the same level of theory, to identify all the stationary points as minima (zero imaginary frequency) or transition states (one imaginary frequency) and to obtain Gibbs free energy corrections at 298.15 K. The concentration correction of 1.9 kcal/mol (derived from the free-energy change of 1 mol of an ideal gas from 1 atm (24.5 L/mol, 298.15 K) to 1 M) at 298.15 K was added for all species except water, for which 4.3 kcal/mol is used as the standard state of the water solvent is 55.6 M. Unless otherwise mentioned, we report the B3LYP*-D3 energies including Gibbs free energy corrections and D3 dispersion from B3LYP.

To construct the energy diagram for the full catalytic cycle, the total exergonicity of 50.6 kcal/mol derived from the experimental overpotential (1.72 V for Ce^{IV}/Ce^{III}, and 1.171 V for water oxidation at pH = 1) was used. By using this experimental parameter, the calculated reference energy for proton-coupled electron transfer becomes 407.6 kcal/mol (including correction for the pH of the solution). This approach has been successfully applied in the study of Photosystem II and a number of synthetic water oxidation catalysts.^{33–41} To calculate pK_s of various species, the experimental solvation free energy of a proton (–264.0 kcal/mol, corresponding to 1 atm in the gas phase and 1 M in the solution phase) was used.³² In this methodology, the reference energy for one electron oxidation was estimated to be 135.9 kcal/mol. Compared to the absolute redox potential of the Ce⁴⁺/Ce³⁺ couple (1.72 + 4.281 V),⁴² which corresponds to an electron affinity of 138.4 kcal/mol, an error of 2.5 kcal/mol (0.108 V) is present for each oxidation step. For B3LYP*, B3LYP-D3, M06-D3, M06L-D3, and PBE1PBE-D3, the errors are 2.5, 1.0, 1.7, 3.7, and 3.7 kcal/mol, respectively. For more details on calculating redox potentials and pK_s, see Supporting Information. The uncertainties of density functionals for the calculations of absolute redox potentials and pK_a have been shown to be around 0.2 V and 3 units, respectively.^{43,44}

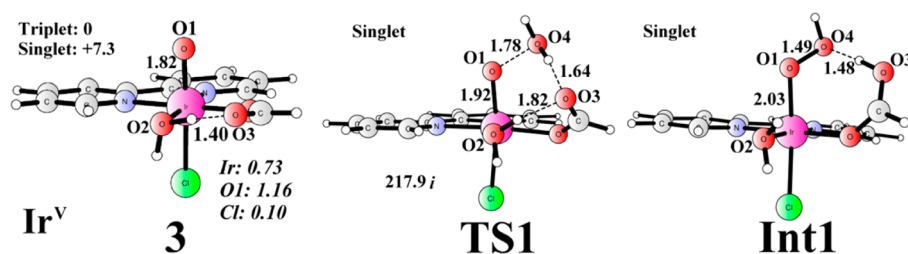


Figure 2. Optimized structures of **3**, transition state (**TS1**), and intermediate (**Int1**) for O–O bond formation at Ir^V. Distances are given in Å. Spin densities on selected atoms of **3** are indicated in italics. The imaginary frequency of **TS1** is also shown. Relative energies of different spin states of **3** are given in kcal/mol.

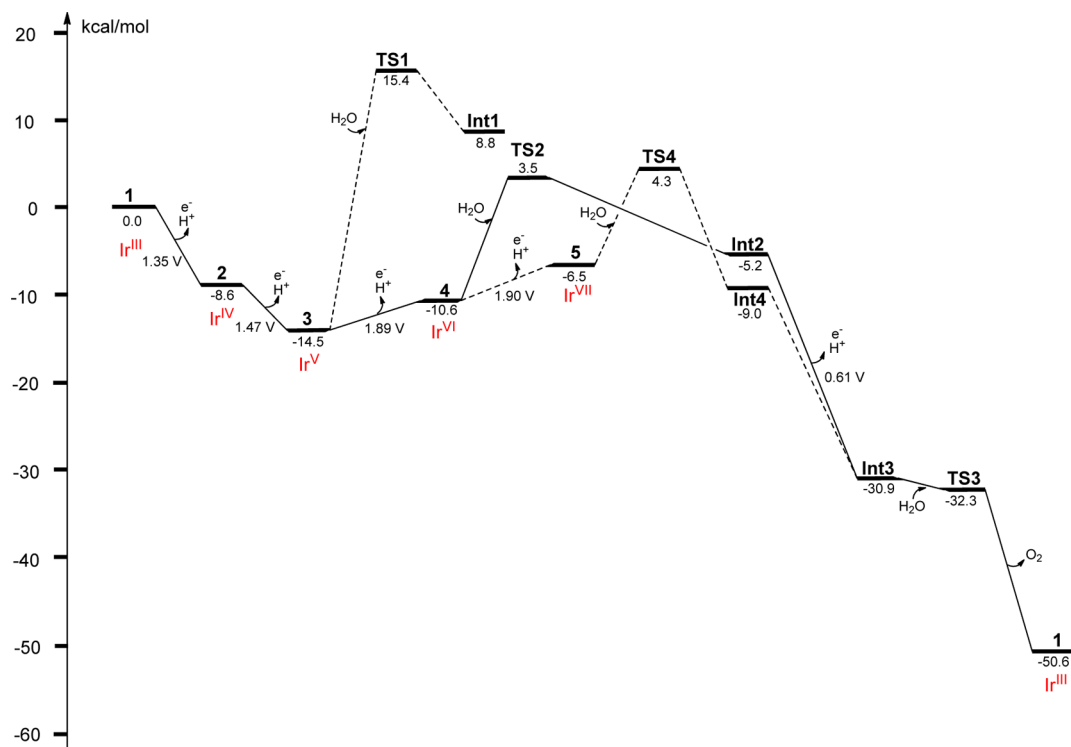


Figure 3. Energy diagrams for water oxidation by $[(\text{bpy})\text{Ir}^{\text{III}}(\text{H}_2\text{O})_2(\text{HCOO})\text{Cl}]^+$.

Table 1. Comparison of Redox Potentials and Barriers Calculated Using Different Density Functionals

| | | redox potentials (in V) | | | | | total barrier (in kcal/mol) | | |
|---------|------------|-------------------------|--------------|--------------|----------------|---------------------------|-----------------------------|--------|---------|
| | | Ir(IV)/Ir(III) | Ir(V)/Ir(IV) | Ir(VI)/Ir(V) | Ir(VII)/Ir(VI) | Ir–O ₂ /Ir–OOH | Ir(V) | Ir(VI) | Ir(VII) |
| formate | B3LYP*-D3 | 1.35 | 1.47 | 1.89 | 1.90 | 0.61 | 29.9 | 18.0 | 18.8 |
| | B3LYP* | 1.32 | 1.44 | 1.86 | 1.86 | 0.58 | 33.4 | 21.2 | 20.9 |
| | B3LYP-D3 | 1.40 | 1.50 | 2.00 | 1.93 | 0.52 | 31.3 | 22.3 | 22.2 |
| | M06-D3 | 1.48 | 1.56 | 1.97 | 1.97 | 0.43 | 30.8 | 24.0 | 26.7 |
| | M06L-D3 | 1.33 | 1.39 | 1.75 | 1.69 | 0.46 | 30.6 | 15.4 | 14.6 |
| | PBE1PBE-D3 | 1.50 | 1.56 | 2.14 | 2.05 | 0.49 | 32.6 | 27.5 | 28.3 |
| acetate | B3LYP*-D3 | 1.36 | 1.52 | 1.85 | 1.83 | 0.74 | 27.6 | 14.7 | 16.3 |
| | B3LYP* | 1.33 | 1.48 | 1.82 | 1.79 | 0.70 | 31.6 | 18.3 | 18.7 |
| | B3LYP-D3 | 1.41 | 1.55 | 1.95 | 1.87 | 0.66 | 29.2 | 19.0 | 19.9 |
| | M06-D3 | 1.49 | 1.60 | 1.95 | 1.90 | 0.57 | 29.2 | 20.9 | 24.5 |
| | M06L-D3 | 1.34 | 1.44 | 1.72 | 1.60 | 0.62 | 27.9 | 11.5 | 14.5 |
| | PBE1PBE-D3 | 1.50 | 1.61 | 2.09 | 2.00 | 0.62 | 30.8 | 24.7 | 26.3 |

be 29.9 kcal/mol in the singlet state (Figure 3). The triplet state is not a viable option because the triplet product (Ir^{III}) is very high in energy. This is similar to the previous investigation using an unmodified Cp* ligand, in which O–O bond formation takes place via the singlet state.¹⁶ The present

barrier is somewhat lower due the presence of formate as a general base, while in the previous study, a proton is transferred to the water solvent. Compared with experimental kinetic data, which gave a barrier of about 18 kcal/mol, the calculated barrier is overestimated by around 10 kcal/mol. One might suspect

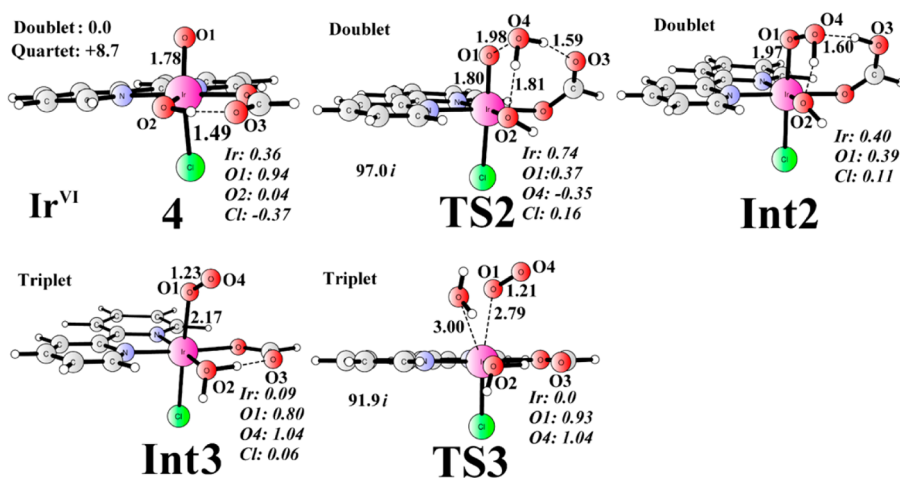


Figure 4. Optimized structures of **4**, transition states, and intermediates for O–O bond formation and O₂ release. Distances are given in Å. Spin densities on selected atoms are indicated in italics. The imaginary frequencies of TS2 and TS3 are also shown.

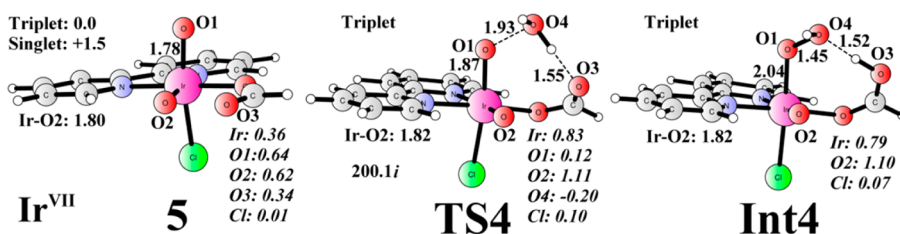


Figure 5. Optimized structures of **5**, transition state (TS4), and intermediate (Int4) for O–O bond formation at Ir^{VII}. Distances are given in Å. Spin densities on selected atoms are indicated in italics. The imaginary frequency of TS4 is also shown. Relative energies of different spin states of **5** are given in kcal/mol.

that the error comes from the density functional used. However, we also tested a number of other popular density functionals, including B3LYP* (excluding dispersion), B3LYP-D3, M06-D3, M06L-D3, and PBE1PBE-D3 (Table 1), and found that they gave similar barriers, all around 30 kcal/mol.

An alternative scenario is that the mechanism is not correct. Indeed, we found that it is possible to undergo further PCET oxidation to form an Ir^{VI} complex **4** (Figure 4), which can then promote O–O bond formation. The redox potential for the Ir^{VI}/Ir^V transition was calculated to be 1.89 V, slightly higher than the reference Ce^{IV}/Ce^{III} potential (1.72 V). This oxidation process is thus endergonic by 3.9 kcal/mol. **4** can be characterized as an Ir^V-oxyl radical, which is a doublet, with the quartet lying 8.7 kcal/mol higher in energy. O–O bond formation takes place in the doublet state via TS2 (Figure 4), which has a barrier of 14.1 kcal/mol relative to **4**. The total barrier is thus 18.0 kcal/mol when the energetic penalty for the oxidative formation of **4** is added. Compared with that from Ir^V, the barrier for O–O bond formation at Ir^{VI} is 11.9 kcal/mol lower. The main reason is that the oxidation power of Ir^{VI} is higher than that of Ir^V. Consequently, electron transfer to the metal during the water attack is more favored for Ir^{VI} than Ir^V. This is also evidenced by the large energy penalty for the formation of the peroxide intermediate (Int1 for Ir^V and Int2 for Ir^{VI}). At Ir^V, the formation of the O–O bond is endergonic by as much as 23.3 kcal/mol, while only 5.4 kcal/mol for Ir^{VI}. At TS2, the nascent O1–O4 bond is 1.78 Å, and the Ir–O1 bond is elongated from 1.82 Å at **4** to 1.92 Å at TS2. The incoming water molecule delivers a proton to the formate, with a distance of 1.59 Å between the water proton and the formate oxygen. In addition, a hydrogen bond (with a distance of 1.81

Å) is seen between the water and the equatorial hydroxide, which may facilitate the attack. From Int2, PCET oxidation leads to the formation of a triplet Ir^{III}–O₂ intermediate Int3, which can undergo very facile ligand exchange with a water molecule to liberate the O₂ molecule (via TS3) to regenerate **1**.

We have also considered further PCET oxidation of **4** to generate a formally Ir^{VII} complex **5** (Figure 5). The redox potential was calculated to be 1.90 V, which is very close to that for the Ir^{VI}/Ir^V transition. The electronic structure of **5** can be interpreted as an Ir^V dioxy complex with a triplet ground state. The broken-symmetry singlet, closed-shell singlet, and quintet are 1.5, 9.8, and 14.7 kcal/mol higher in energy, respectively. The transition state (TS4) for the water attack on the axial oxyl radical has been optimized and is shown in Figure 5. The barrier was calculated to be 10.8 kcal/mol relative to **5**, however, the total barrier becomes 18.8 kcal/mol relative to **3**. This is only 0.8 kcal/mol higher than that from Ir^{VI}, which is a too small difference for drawing safe conclusion about the question whether O–O bond formation takes place at Ir^{VI} or Ir^{VII}. Single-point calculations using other functionals also give quite close barriers. The total barrier differences are 0.1, 2.7, 0.8, and 0.8 kcal/mol, respectively, at the B3LYP-D3, M06-D3, M06L-D3, and PBE1PBE-D3 levels, respectively. Importantly, the barriers for the O–O bond formation at Ir^V are all significantly higher for all functionals used. For example, at the M06-D3 level, the barrier at Ir^V is 30.8 kcal/mol, while it is 24.0 kcal/mol at Ir^{VI}, 6.8 kcal/mol lower.

Under highly oxidative conditions (large amount of Ce^{IV}), one might expect that the formate ligand can be oxidized to release carbon dioxide. We have considered this reaction pathway (structures see Supporting Information Figure S16),

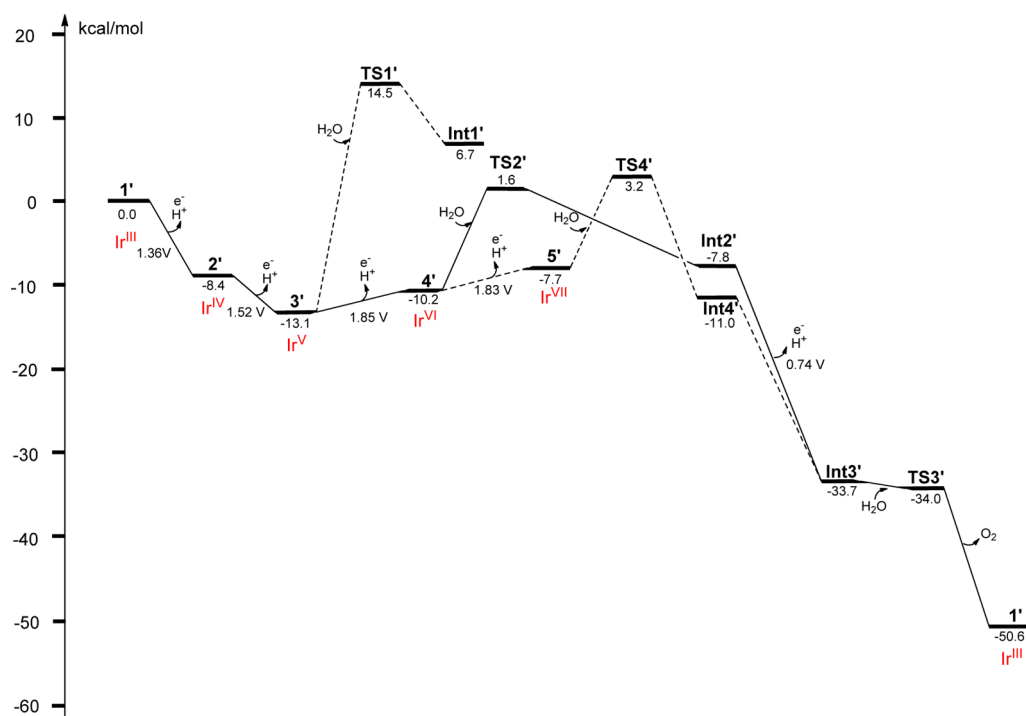
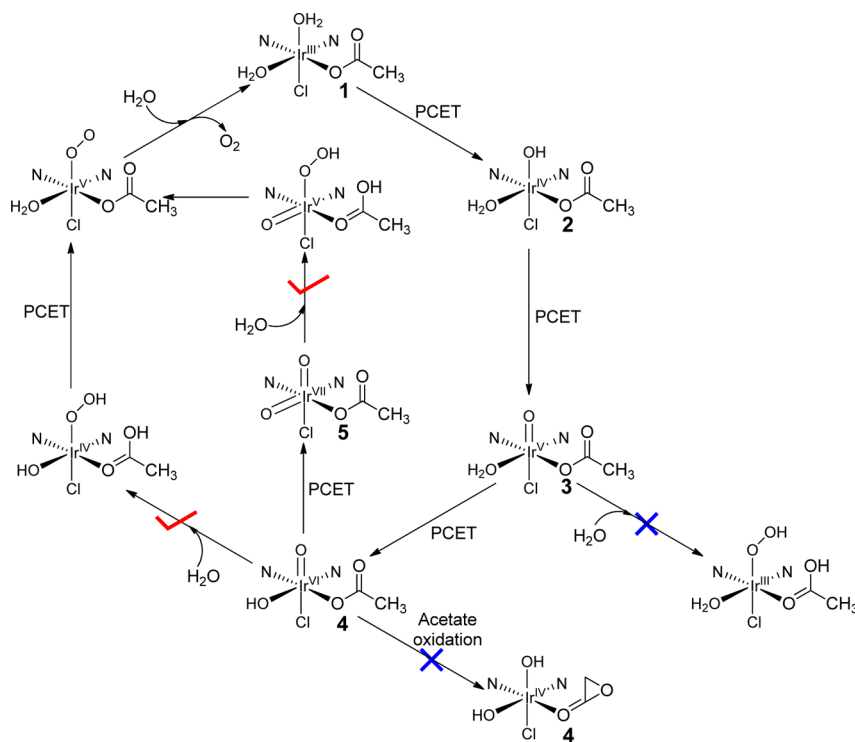


Figure 6. Energy diagrams for water oxidation by $[(\text{bpy})\text{Ir}^{\text{III}}(\text{H}_2\text{O})_2(\text{CH}_3\text{COO})\text{Cl}]^+$.

Scheme 3. Pathways Considered for Catalyst 1'



and it turns out that this pathway has an even lower barrier (14.9 kcal/mol) than the desired water oxidation pathway (18.0 kcal/mol). Therefore, $[(\text{bpy})\text{Ir}^{\text{III}}(\text{H}_2\text{O})_2(\text{HCOO})\text{Cl}]^+$ proposed on the basis of MS cannot account for the activity of this catalyst.

3.2. Water Oxidation Catalyzed by $[(\text{bpy})\text{Ir}^{\text{III}}(\text{H}_2\text{O})_2(\text{CH}_3\text{COO})\text{Cl}]^+$. As shown in the introduction, acetate is also formed during the oxidation of the Cp^* ligand. Even

though it was not seen bound to the metal in the MS, we cannot exclude the possibility of its coordination in solution and thus contributing to the catalytic activity. Importantly, the concentration of acetate (1.8× of that of Cp^*) was found to be much larger than that of formate (less than 5% of that of Cp^*) after adding 30 equiv of CAN.²³ When more CAN is added, all formate will be consumed. For comparison, the structures shown in Figure 3 were chosen to be reoptimized with acetate.

Exchange of formate in **1** by acetate to form $[(\text{bpy})\text{Ir}^{\text{III}}(\text{H}_2\text{O})_2(\text{CH}_3\text{COO})\text{Cl}]^+$ (labeled as **1'**) was calculated to be endergonic by 1.1 kcal/mol. This could explain why only the complex with formate coordinated were observed in the MS,²³ as formate binds slightly stronger to Ir compared with acetate. For convenience, all other optimized structures for acetate are labeled with prime (') as compared with the structures for formate. The full energy diagram for $[(\text{bpy})\text{Ir}^{\text{III}}(\text{H}_2\text{O})_2(\text{CH}_3\text{COO})\text{Cl}]^+$ is presented in Figure 6, from which one can compare the relative reactivity of **1** and **1'**. In addition, a full catalytic cycle for catalyst **1'** is shown in Scheme 3, which can be compared with that for **1** in Scheme 2.

1' follows the same reaction mechanism as **1**. The calculated redox potentials of all oxidation steps were quite close between acetate and formate, with typical differences of less than 0.15 V (Table 1). In addition, the barriers for O–O bond formation are slightly lower for acetate compared with formate. For example, the barrier for water attack at Ir^{VI} for acetate was calculated to be 14.7 kcal/mol at the B3LYP*-D3 level, which is 3.3 kcal/mol lower than that for formate. Similar trends were found when other functionals were used. Two possible reasons can be identified. First, acetic acid has a pK_a of 4.76, which is higher than that of formic acid (3.75),⁴⁵ and acetate is therefore a slightly better base to abstract proton during the water attack. Consequently, the formation of the peroxide is less endergonic for acetate (+2.4 kcal/mol) than that for formate (+5.4 kcal/mol). Second, the cost for the generation of Ir^{VI} is also less for acetate (2.9 kcal/mol) than that for formate (3.9 kcal/mol). These two important factors explain the different reactivity of the Ir catalyst with acetate and formate. Importantly, the calculated barriers at Ir^V are also much higher than those at Ir^{VI} and Ir^{VII}. Furthermore, for all functionals used, the barriers at Ir^{VI} are slightly lower than those at Ir^{VII}. Compared with experimental kinetic data (about 18 kcal/mol), B3LYP*-D3 and M06L-D3 underestimates the barrier slightly, while B3LYP-D3 and M06-D3 gave excellent agreement, and PBE1PBE-D3 overestimates the barrier somewhat.

We also considered acetate oxidation from **4'** (structures see Supporting Information Figure S17). Different from the formate case, acetate oxidation by hydride transfer has a barrier of 20.5 kcal/mol from **4'**, resulting in a total barrier of 23.4 kcal/mol. This is 8.7 kcal/mol higher than that for water oxidation. These results suggest that $[(\text{bpy})\text{Ir}^{\text{III}}(\text{H}_2\text{O})_2(\text{CH}_3\text{COO})\text{Cl}]^+$ is a likely precatalyst.

Very recently, the mechanism for water oxidation catalyzed by an Iridium carbene complex has also been reported using DFT calculations.⁴⁶ Both Ir^V and Ir^{VI} have been considered to promote O–O bond formation via water attack. However, the barriers for the water attack mechanism at both Ir^V and Ir^{VI} were calculated to be more than 30 kcal/mol at the M06 level. The alternative direct O–O coupling mechanism at Ir^{VII} has also been considered but was associated with a barrier of 31.4 kcal/mol. Here we also considered the direct coupling mechanism of two oxygen atoms from the Ir^{VII} species **5'**. The optimized transition state is shown in Supporting Information Figure S18, and the barrier was calculated to be 38.3 kcal/mol relative to **5'** at the B3LYP*-D3 level. Single-point calculation using M06 also gave a very high barrier of 47.3 kcal/mol. This suggests that the direct coupling mechanism is not a viable option, at least for the present catalyst.

3.3. Water Oxidation Catalyzed by $[(\text{bpy})\text{Ir}^{\text{III}}(\text{H}_2\text{O})_3\text{Cl}]^{2+}$. In order to understand the effect of acetate on the catalytic activity, acetate is replaced by an aqua ligand,

which is endergonic by 6.8 kcal/mol at Ir^{III}. In this case, the pK_a of the complex is shifted, and the major species at pH = 1 is $[(\text{bpy})\text{Ir}^{\text{III}}(\text{H}_2\text{O})_3\text{Cl}]^{2+}$ (pK_a = 7.1, Figure 7, Figure S4 and

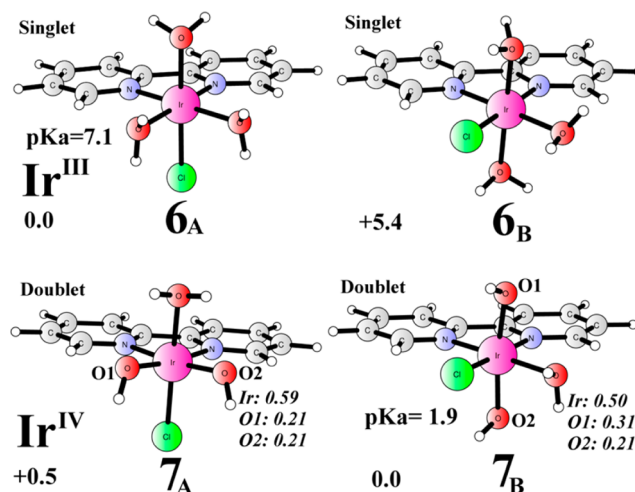


Figure 7. Optimized isomers of **6** and **7**. Distances are given in Å. Spin densities on selected atoms are indicated in italics.

S19). Two possible isomers can be envisioned, which are labeled as **6_A**, with the chloride ligand on the axial position, and **6_B**, with the chloride ligand on the equatorial position. The energy of **6_B** is 5.4 kcal/mol higher than that of **6_A**. Dissociation of one water molecule from **6_A** was calculated to be endergonic by 5.5 kcal/mol (Figure S20). Exchange of the chloride ligand by a water ligand in **6_A** was found to be endergonic by 18.7 kcal/mol (Figure S21). These results suggest that **6_A** is the dominant species at the Ir^{III} stage.

Under experimental condition (pH = 1), the one electron oxidation of both **6_A** and **6_B** was calculated to be coupled with the release of two protons, thus generating $[(\text{bpy})\text{Ir}^{\text{IV}}(\text{H}_2\text{O})(\text{OH})_2\text{Cl}]^+$. The resulting species are labeled as **7_A** and **7_B** (Figure 7, Figures S22–S24), respectively. Unexpectedly, the energy of **7_B** is lower by 0.5 kcal/mol than **7_A**. Both **7_A** and **7_B** are low-spin doublet, with partial spin delocalization on the two hydroxide ligands. The redox potentials for the **7_A/6_A** and **7_B/6_B** transitions were calculated to be 1.41 and 1.15 V, respectively (energy diagrams see Figure 8 and 9). We found that **7_A** and **7_B** can interconvert by dissociation of a water ligand and via an isomerization transition state (**7-TS_{iso}**, Figures S25 and S26). The total barrier is only 9.6 kcal/mol relative to **7_A**, suggesting a very fast process. The pK_a of **7_B** is 1.9, and the pK_a of the protonated form (**7_{pt-A}**, Figure S22) is –1.3.

The next oxidation is a PCET process, leading to the formation of $[(\text{bpy})\text{Ir}^{\text{V}}\text{O}(\text{OH})(\text{OH}_2)\text{Cl}]^+$. The two isomers are labeled as **8_A** and **8_B** (Figure 10, Figures S27–S33), respectively. **8_B** is lower in energy by 1.6 kcal/mol, suggesting that **8_B** is the major form at the Ir^V stage. The redox potentials were calculated to be 1.48 and 1.43 V, respectively, for the **8_A/7_A** and **8_B/7_B** transitions, respectively. The ground state of **8_A** and **8_B** is triplet, and a spin analysis suggests that the electronic structure can be described as an Ir^{IV}-oxyl complex. Interconversion between **8_A** and **8_B** is also very facile, with a total barrier of 7.9 kcal/mol relative to **8_A** (Figures S30 and S31). From **8_A** and **8_B**, O–O bond formation can proceed by water attack on the oxyl radical, facilitated by the hydroxide ligand, which abstracts a proton during the attack. The two transition states (**TSS_A** and **TSS_B**) optimized are shown in

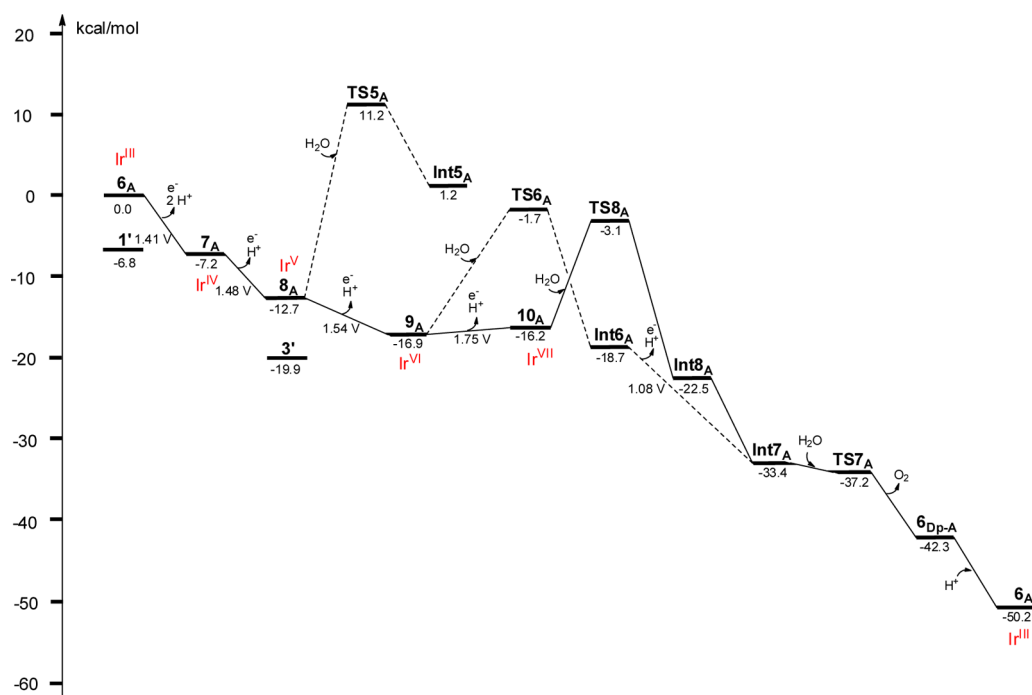


Figure 8. Energy diagram for water oxidation by $[(\text{bpy})\text{Ir}^{\text{III}}(\text{H}_2\text{O})_3\text{Cl}]^{2+}$ in isomer A.

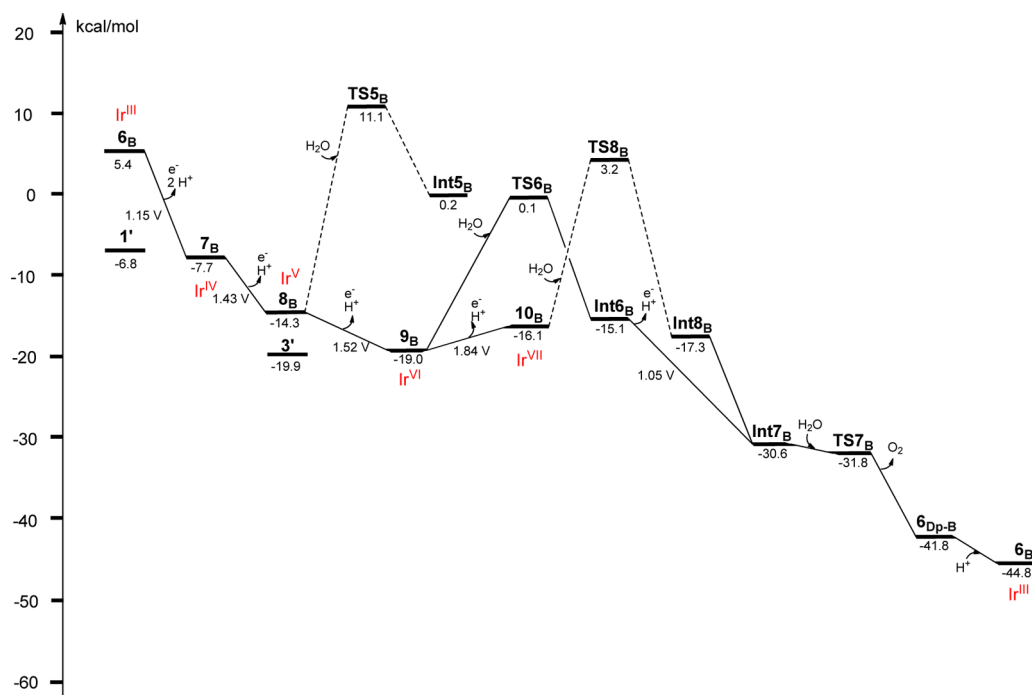


Figure 9. Energy diagram for water oxidation by $[(\text{bpy})\text{Ir}^{\text{III}}(\text{H}_2\text{O})_3\text{Cl}]^{2+}$ in isomer B.

Figure 10. Similarly to the acetate ligated catalyst, the resulting Ir^{III} product is a singlet and O–O bond formation can only take place via the singlet state. The barriers were calculated to be 25.5 and 25.4 kcal/mol relative to 8_{B} , respectively, for TS5_{A} and TS5_{B} , respectively. If the energy cost for the exchange of acetate to hydroxide is added (5.6 kcal/mol, Figure 9), the total barriers became more than 30 kcal/mol. The barriers are much higher compared to the barrier derived from the experimental kinetic data (around 18 kcal/mol). Single-point calculations using other density functionals, including B3LYP-D3, M06-D3,

M06L-D3, and PBE1PBE-D3, gave barriers in the range of 28–32 kcal/mol (energy cost for ligand exchange not included, see Table 2 for details), which are too high to account for the observed activity. However, as discussed below, further oxidation to Ir^{VI} or even Ir^{VII} can further lower the barrier. A comparison of the O–O bond formation and interconversion is shown in Figure 11. At Ir^{V} , the barrier for the interconversion is much lower compared with O–O bond formation, and therefore, it will not affect the total barrier for the O–O bond formation. As the $\text{p}K_{\text{a}}$ of 8_{B} was calculated to be 1.3, it

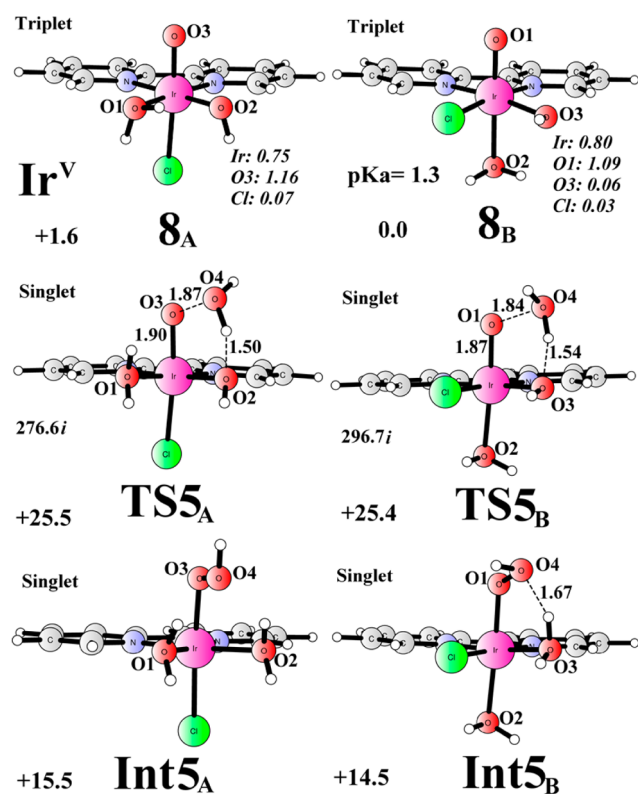


Figure 10. Optimized isomers of **8**, transition state (**TS5**) and intermediate (**Int5**) for O–O bond formation at Ir^V. Distances are given in Å. Spin densities on selected atoms of **8_A** and **8_B** are indicated in italics. The imaginary frequency of **TS5_A** and **TS5_B** is also shown. Energies relative to **8_B** (or **8_B** + H₂O) are given in kcal/mol.

suggests that the cost for the deprotonation of **8_B** is very small, being only 0.4 kcal/mol at pH = 1. We thus tried O–O bond formation from the deprotonated form (Figure S33). However, the calculated barriers are over 30 kcal/mol, ruling out this possibility as well.

Further PCET oxidation can generate a formally Ir^{VI} species (Figures S34–S40). Our calculations show that the redox potentials decrease compared with the acetate ligated case, being 1.54 V for oxidation of **8_A** to **9_A** and 1.52 V for oxidation of **8_B** to **9_B** (Figure 12). These results suggest that the generation of Ir^{VI} complex is exergonic under the experimental catalytic condition (1.72 V for Ce^{IV}/Ce^{III}). **9_B** is lower in energy by 2.1 kcal/mol compared with **9_A**. The ground state of **9_A** and

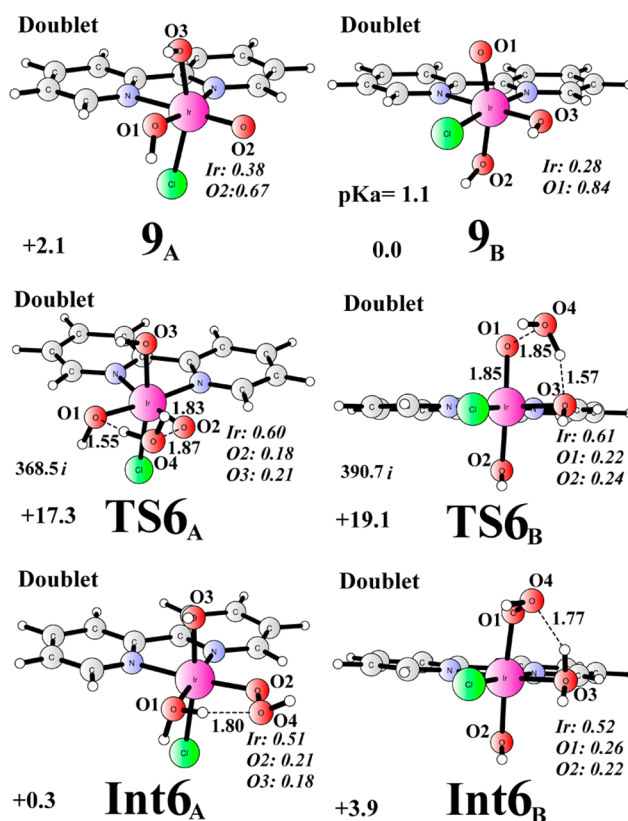


Figure 12. Optimized isomers of **9**, transition state (**TS6**) and intermediate (**Int6**) for O–O bond formation at Ir^{VI}. Distances are given in Å. Spin densities on selected atoms are indicated in italics. The imaginary frequencies of **TS6_A** and **TS6_B** are also shown. Energies relative to **9_B** (or **9_B** + H₂O) are given in kcal/mol.

9_B is a doublet, and the electronic structure can be interpreted as an Ir^V-oxyl complex. From **9_A** and **9_B**, O–O bond formation can proceed via water attack on the oxyl radical, coupled with proton transfer to one of the two hydroxide ligands. The optimized transition states **TS6_A** and **TS6_B** are displayed in Figure 12, and the associated barriers were calculated to be 17.3 and 19.1 kcal/mol relative to **9_B**, respectively. If the energy cost for the acetate hydroxide ligand exchange is included (0.9 kcal/mol, Figure 9), the total barriers became 18.2 and 20.0 kcal/mol, respectively. At **TS6_A**, the distance between the incoming water oxygen (O4) and the oxyl radical (O2) is 1.87 Å, while the distance between the transferred proton and the equatorial

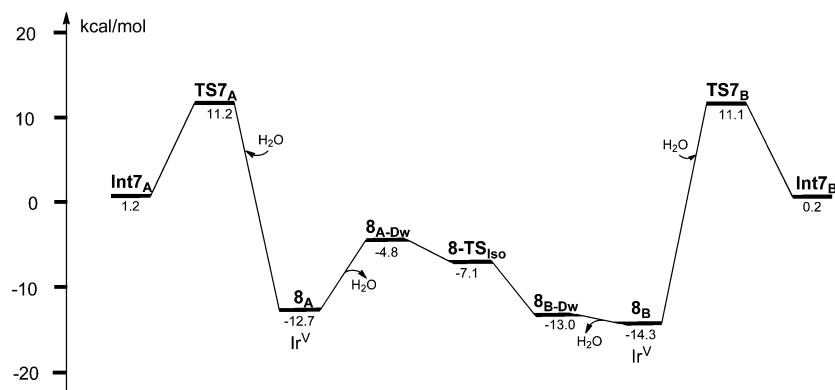


Figure 11. Potential energy profile for the interconversion of **8_A** and **8_B**, and O–O bond formation from **8_A** and **8_B**.

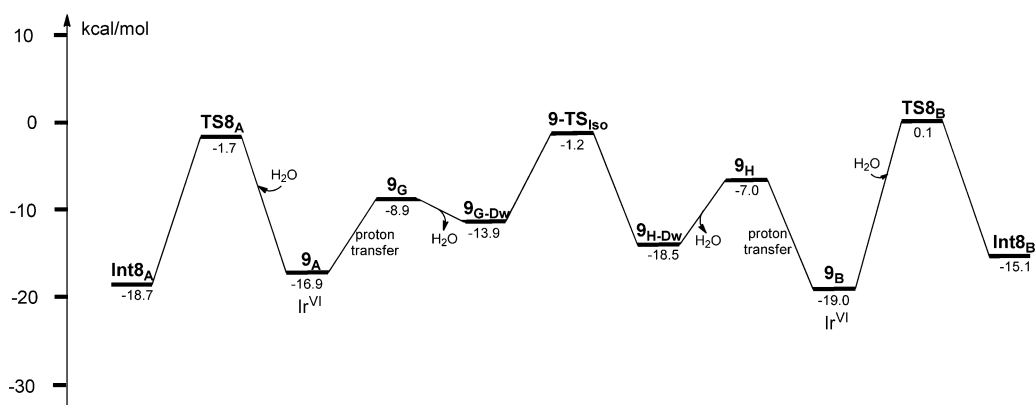


Figure 13. Potential energy profile for the interconversion of 9_A and 9_B , and O–O bond formation from 9_A and 9_B .

hydroxide oxygen (O1) is 1.55 Å. During the attack, one electron goes to the Ir center, as shown by the increase of spin density from 0.38 at 9_A to 0.60 at $TS6_A$. The other electron goes to the oxyl radical to form the O–O bond, which can be seen on the decrease of spin density on O2 (oxyl) from 0.67 at 9_A to 0.18 at $TS6_A$. In order to go from 9_B to $TS6_A$, an isomerization from 9_B to 9_A has to take place first. The potential energy profile for this process is shown in Figure 13 (structures see Figure S38). The total barrier for the isomerization was calculated to be 17.8 kcal/mol, slightly higher than the following O–O bond formation barrier. We also performed single-point calculations using B3LYP-D3, M06-D3, M06L-D3, and PBE1PBE-D3. For all functionals tested, $TS6_A$ gives a lower barrier than $TS6_B$ (Table 2). For $TS6_A$, B3LYP-D3 gives a barrier of 20.3 kcal/mol, while M06-D3 gives a barrier of 25.0 kcal/mol, which is the highest among the tested functionals. As a technical note, it is very important to include dispersion, which can improve the energy by several kcal/mol, as seen from the difference between the B3LYP* and B3LYP*-D3 data. Another important issue is that the barrier for the interconversion becomes much lower when other functionals are used (see Table S3 for details). For example, at the M06-D3 level, the barrier for isomerization is 15.8 kcal/mol, 9.2 kcal/mol lower than that for O–O bond formation via isomer A. Most likely, the interconversion will not contribute to the rate-limiting step. We have also tried O–O bond formation from a deprotonated Ir^{VI} complex, as the pK_a of 9_B was calculated to be 1.1 and it can get deprotonated at pH = 1. However, as shown in Supporting Information (Figure S40), the barrier becomes about 40 kcal/mol, suggesting that only the protonated form 9_A and 9_B is active. At higher pH, the complex needs to become protonated to form 9_A or 9_B to enable O–O bond formation.

O–O bond formation from Ir^{VI} leads to the formation of an Ir^{IV}-peroxide intermediate ($Int6_A$ and $Int6_B$), from which PCET can take place to form an Ir^{IV}-superoxide intermediate ($Int7_A$ and $Int7_B$). The redox potentials for the $Int7_A/Int6_A$ and $Int7_B/Int6_B$ transitions were calculated to be 1.08 and 1.05 V, respectively. The ground states of $Int7_A$ and $Int7_B$ were found to be broken-symmetry singlets. For $Int7_A$, the triplet and the closed-shell singlet are 1.2 and 5.0 kcal/mol higher in energy, respectively. From $Int7_A$ and $Int7_B$, O₂ can be released from the Ir center, which is coupled with the binding of a water molecule. This step was found to be barrierless, and the corresponding transition states ($TS7_A$ and $TS7_B$) are shown in Figure 14. This is followed by protonation of the complex to

regenerate the starting complex 6_A and 6_B for the next catalytic cycle.

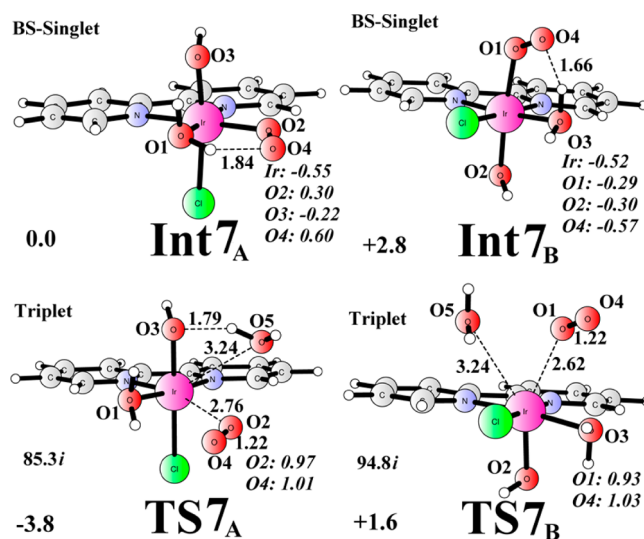


Figure 14. Optimized structures of intermediate and transition state for O₂ release. Distances are given in Å. Spin densities on selected atoms are indicated in italics. The imaginary frequency of $TS7$ is also shown.

From the Ir^{VI} complex, it is also possible to undergo one further PCET oxidation to generate a formally Ir^{VII} complex (10_A and 10_B , Figure 15, Figures S41–45). The redox potentials for the formal Ir^{VII}/Ir^{VI} couple were calculated to be 1.75 and 1.84 V, for 10_A and 10_B , respectively. These values are slightly higher than the reference Ce^{IV}/Ce^{III} couple (1.72 V), suggesting a slightly endergonic process. Both 10_A and 10_B have significant oxyl radical characters, and their electronic structures can be interpreted as a mixture of Ir^{VI}-oxyl and Ir^V-dioxy. The pK_a of 10_A was calculated to be 0.2, suggesting that 10_A should be deprotonated at pH = 1 (total charge of 0). However, as shown in the Supporting Information (Figure S45), the barrier is much higher compared to its protonated (total charge of +1) form, and therefore, only the results for the protonated form are shown here. 10_A and 10_B are very close in energy, with a difference of only 0.1 kcal/mol. It should be pointed out that they cannot interconvert directly as no water molecule can be eliminated from 10_A and 10_B to create an empty site for isomerization. The most likely pathway for the interconversion is therefore first a reduction to Ir^{VI}, followed by

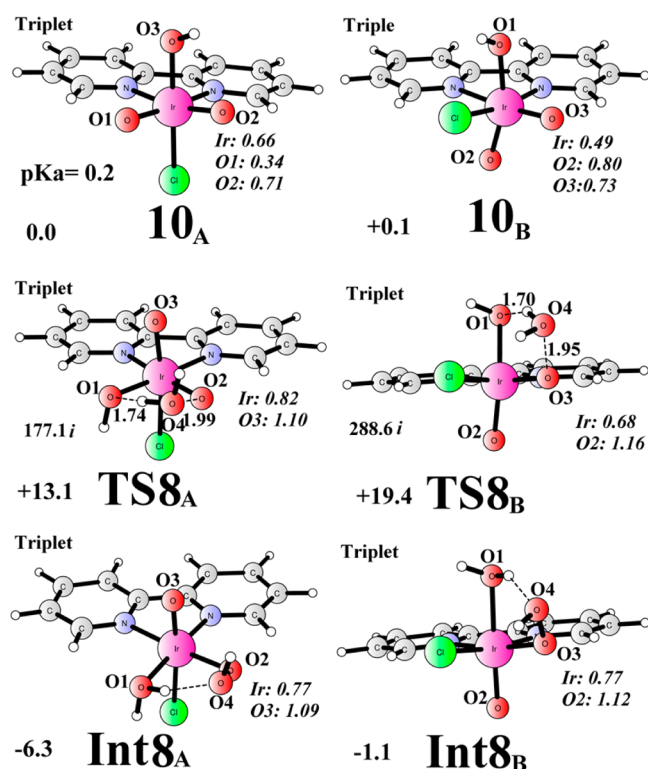


Figure 15. Optimized isomers of 10, transition state (TS8) and intermediate (Int8) for O–O bond formation at Ir^{VII}. Distances are given in Å. Spin densities on selected atoms are indicated in italics. The imaginary frequency of TS8_A and TS8_B is also shown. Energies relative to 10_B (or 10_B + H₂O) are given in kcal/mol.

an interconversion at Ir^{VI}, and by a reoxidation. The optimized structures for the O–O bond formation transition state (TS8_A and TS8_B) and the resulting intermediates (Int8_A and Int8_B) are shown in Figure 15. The barriers were calculated to be 13.1 and 19.4 kcal/mol relative to 10_A, for TS8_A and TS8_B, respectively. The total barriers become 16.8 and 24.4 kcal/mol, if the energy penalties for the acetate hydroxide ligand exchange and the Ir^{VII}/Ir^{VI} transition are added. For isomer A, the barrier at Ir^{VII} (16.8 kcal/mol) is slightly lower than that at Ir^{VI} (18.2 kcal/mol), and similar results can be seen when the B3LYP-D3,

M06-D3 and M06L-D3 functionals are used (Table 2), while at the PBE1PBE-D3 level the Ir^{VI} pathway is preferred. O–O bond formation via isomer A is always preferred for all functionals used, with a difference in the range of 6–8 kcal/mol favoring TS8_A. From Int8_A and Int8_B, proton transfer from the peroxide to the oxyl group leads to Int7_A and Int7_B, respectively. This is followed by O₂ release and water binding, as discussed above.

By comparing the barriers calculated for Ir^V, Ir^{VI}, and Ir^{VII} (Table 2), it can be seen that the barriers at Ir^V are always higher than that of Ir^{VI} and Ir^{VII}. For B3LYP*-D3, B3LYP-D3, M06-D3, and M06L-D3, Ir^{VII} gave lower barrier, but Ir^{VI} may also contribute to the activity. PBE1PBE-D3 gave the opposite results, which favors the Ir^{VI} pathway, due to the quite high computed redox potentials for the Ir^{VII}/Ir^{VI} transition (2.04 V for isomer A and 1.95 V for isomer B) and to the cost to reach Ir^{VII} is high (5.8 kcal/mol for isomer B). Indeed, PBE1PBE-D3 gave the highest redox potentials for all redox processes studied, except for the Ir-OOH/Ir–O₂ couple with an acetate ligand (Table 1).

4. CONCLUSION

In the present paper, the water oxidation mechanism of Cp*Ir(bpy)Cl has been reinvestigated on the basis of recent experimental findings, which indicate that the catalytic active species might be [(bpy)Ir^{III}(H₂O)₂(HCOO)Cl]⁺. DFT calculations were performed on three potential catalytic species, [(bpy)Ir^{III}(H₂O)₂(HCOO)Cl]⁺, [(bpy)Ir^{III}(H₂O)₂(CH₃COO)Cl]⁺, and [(bpy)Ir^{III}(H₂O)₃Cl]²⁺. Relevant redox intermediates, redox potentials, and reaction pathways for O–O bond formation were calculated and compared. On the basis of these calculations, we propose that the most likely catalytic species is [(bpy)Ir^{III}(H₂O)₂(CH₃COO)Cl]⁺ and O–O bond formation takes place via Ir^{VI} and Ir^{VII}, rather than Ir^V, as proposed before. The whole catalytic cycle is summarized in Scheme 3.

Three sequential PCET oxidations of [(bpy)Ir^{III}(H₂O)₂(HCOO)Cl]⁺ lead to the formation of an Ir^{VI} species, from which O–O bond formation can take place via water attack, associated with a barrier of 18.0 kcal/mol. However, formate oxidation was found to have an even lower barrier, being 14.9 kcal/mol. Even though formate was seen

Table 2. Comparison of Redox Potentials and Barriers for Two Isomers Calculated Using Different Density Functionals

| | | redox potentials (in V) | | | | water oxidation barrier (in kcal/mol) ^a | | | |
|---|------------|-------------------------|--------------|--------------|----------------|--|--------|----------------------|------|
| | | Ir(IV)/Ir(III) | Ir(V)/Ir(IV) | Ir(VI)/Ir(V) | Ir(VII)/Ir(VI) | Ir(V) | Ir(VI) | Ir(VII) ^b | |
| A | B3LYP*-D3 | 1.41 | 1.48 | 1.54 | 1.75 | 1.08 | 25.5 | 17.3 | 15.9 |
| | B3LYP* | 1.34 | 1.45 | 1.52 | 1.72 | 1.06 | 28.6 | 20.3 | 18.6 |
| | B3LYP-D3 | 1.51 | 1.51 | 1.66 | 1.79 | 1.08 | 30.3 | 21.2 | 17.6 |
| | M06-D3 | 1.55 | 1.55 | 1.64 | 1.89 | 1.09 | 32.2 | 25.0 | 22.7 |
| | M06L-D3 | 1.44 | 1.42 | 1.42 | 1.63 | 1.02 | 31.0 | 22.5 | 18.0 |
| | PBE1PBE-D3 | 1.56 | 1.57 | 1.82 | 1.89 | 1.10 | 31.4 | 22.0 | 25.2 |
| B | B3LYP*-D3 | 1.15 | 1.43 | 1.52 | 1.84 | 1.05 | 25.4 | 19.1 | 23.5 |
| | B3LYP* | 1.10 | 1.41 | 1.48 | 1.82 | 1.00 | 28.1 | 22.3 | 25.2 |
| | B3LYP-D3 | 1.26 | 1.46 | 1.63 | 1.75 | 1.43 | 30.2 | 23.0 | 23.8 |
| | M06-D3 | 1.32 | 1.48 | 1.61 | 1.82 | 1.47 | 31.0 | 26.6 | 29.5 |
| | M06L-D3 | 1.19 | 1.33 | 1.43 | 1.64 | 1.45 | 29.9 | 24.7 | 24.3 |
| | PBE1PBE-D3 | 1.33 | 1.54 | 1.74 | 1.95 | 1.51 | 30.8 | 23.3 | 33.2 |

^aBarrier relative to the lowest isomer; energy cost for the exchange of acetate by hydroxide is not included. ^bBarrier relative to 9 (Ir^{VI}) if the Ir(VII)/Ir(VI) transition is endergonic.

coordinated to Ir in the MS, this species cannot account for the observed water oxidation activity.

$[(\text{bpy})\text{Ir}^{\text{III}}(\text{H}_2\text{O})_2(\text{CH}_3\text{COO})\text{Cl}]^+$ is the most likely pre-catalyst as acetate is also generated during the Cp^* oxidation. Two sequential PCET oxidations of $[(\text{bpy})\text{Ir}^{\text{III}}(\text{H}_2\text{O})_2(\text{CH}_3\text{COO})\text{Cl}]^+$ lead to the formation of an Ir^{V} complex $[(\text{bpy})\text{Ir}^{\text{V}}(\text{H}_2\text{O})(\text{CH}_3\text{COO})\text{Cl}]^+$. Ir^{V} was previously believed to be the key oxidant for O–O bond formation. The barrier for the water attack at Ir^{V} , assisted by the acetate ligand functioning as a general base, turns out to be around 30 kcal/mol using different functionals, which is too high to account for the observed activity. Instead, further PCET oxidations to Ir^{VI} and Ir^{VII} are associated with quite small energetic costs, while the corresponding barrier for the following O–O bond formation decreases significantly compared to that starting from Ir^{V} . The total barriers at the B3LYP*-D3 level are 14.7 and 16.3 kcal/mol, respectively, for Ir^{VI} and Ir^{VII} , respectively. The calculated barriers are in good agreement with the experimental kinetic study, which gave a barrier of around 18 kcal/mol. Water attack at Ir^{VI} leads to the formation of an Ir^{IV} -peroxide intermediate, which is followed by PCET to generate an $\text{Ir}^{\text{III}}\text{--O}_2$ intermediate. Finally, O_2 is released concomitant with the binding of another water molecule to regenerate the starting Ir^{III} complex. Acetate oxidation by C–H activation was found to have much higher barrier (23.4 kcal/mol).

When acetate is not coordinated to the metal, an aqua ligand can occupy this coordination site. Two possible isomers of $[(\text{bpy})\text{Ir}^{\text{III}}(\text{H}_2\text{O})_3\text{Cl}]^{2+}$, labeled as A (with chloride in an axial position) and B (with chloride in an equatorial position), have been found to play an important role in the subsequent water oxidation. Interconversion between A and B can take place at different oxidation levels except Ir^{VII} . The first oxidation of $[(\text{bpy})\text{Ir}^{\text{III}}(\text{H}_2\text{O})_3\text{Cl}]^{2+}$ is coupled with the release of two protons to generate $[(\text{bpy})\text{Ir}^{\text{IV}}(\text{H}_2\text{O})(\text{OH})_2\text{Cl}]^+$. Sequential PCET oxidations can generate Ir^{V} , Ir^{VI} and Ir^{VII} complexes. O–O bond formation by a water attack, assisted by a hydroxide ligand acting as a general base, has a higher barrier for Ir^{V} compared to Ir^{VI} and Ir^{VII} . The barriers for Ir^{VI} and Ir^{VII} are quite close using different functionals, and all functionals prefer Ir^{VII} by a number of kcal/mol except PBE1PBE-D3, which favors the Ir^{VI} pathway by 3.2 kcal/mol. This is different from those with acetate, in which the Ir^{VI} pathway is slightly preferred. The barriers for water oxidation catalyzed by $[(\text{bpy})\text{Ir}^{\text{III}}(\text{H}_2\text{O})_3\text{Cl}]^{2+}$ are higher than that by $[(\text{bpy})\text{Ir}^{\text{III}}(\text{H}_2\text{O})_2(\text{CH}_3\text{COO})\text{Cl}]^+$.

The involvement of Ir^{VI} and Ir^{VII} for O–O bond formation may stimulate further experimental studies to verify the present proposal and to design more efficient catalysts on the basis of this new mechanism.

■ ASSOCIATED CONTENT

Supporting Information

Structures, energy diagram for interconversion, and Cartesian coordinates. This material is available free of charge via the Internet at <http://pubs.acs.org>.

■ AUTHOR INFORMATION

Corresponding Authors

*E-mail: rongzhen@organ.su.se.

*E-mail: ps@organ.su.se.

Notes

The authors declare no competing financial interest.

■ ACKNOWLEDGMENTS

We acknowledge the Swedish Research Council and the Knut and Alice Wallenberg Foundation for financial support. Computer time was generously provided by the Swedish National Infrastructure for Computing. We thank Prof. Robert H. Crabtree for valuable discussion.

■ REFERENCES

- (1) Gust, D.; Moore, T. A.; Moore, A. L. *Acc. Chem. Res.* **2009**, *42*, 1890–1898.
- (2) Cook, T. R.; Dogutan, D. K.; Reece, S. Y.; Surendranath, Y.; Teets, T. S.; Nocera, D. G. *Chem. Rev.* **2010**, *110*, 6474–6502.
- (3) Gersten, S. W.; Samuels, G. J.; Meyer, T. J. *J. Am. Chem. Soc.* **1982**, *104*, 4029–4030.
- (4) Duan, L.; Bozoglian, F.; Mandal, S.; Stewart, B.; Privalov, T.; Llobet, A.; Sun, L. *Nat. Chem.* **2012**, *4*, 418–423.
- (5) McDaniel, N.; Coughlin, F. J.; Tinker, L. L.; Bernhard, S. *J. Am. Chem. Soc.* **2008**, *130*, 210–217.
- (6) Hull, J. F.; Balcells, D.; Blakemore, J. D.; Incarvito, C. D.; Eisenstein, O.; Brudvig, G. W.; Crabtree, R. H. *J. Am. Chem. Soc.* **2009**, *131*, 8730–8731.
- (7) Santoni, M.-P.; La Ganga, G.; Nardo, V. M.; Natali, M.; Puntoriero, F.; Scandola, F.; Campagna, S. *J. Am. Chem. Soc.* **2014**, *136*, 8189–8192.
- (8) Limburg, J.; Vrettos, J. S.; Liable-Sands, L. M.; Rheingold, A. L.; Crabtree, R. H.; Brudvig, G. W. *Science* **1999**, *283*, 1524–1527.
- (9) Karlsson, E. A.; Lee, B.-L.; Åkermark, T.; Johnston, E. V.; Kärkäs, M. D.; Sun, J.; Hansson, Ö.; Bäckvall, J.-E.; Åkermark, B. *Angew. Chem., Int. Ed.* **2011**, *50*, 11715–11718.
- (10) Ellis, W. C.; McDaniel, N. D.; Bernhard, S.; Collins, T. J. *J. Am. Chem. Soc.* **2010**, *132*, 10990–10991.
- (11) Fillol, J. L.; Codolà, Z.; Garcia-Bosch, I.; Gómez, L.; Pla, J. J.; Costas, M. *Nat. Chem.* **2011**, *3*, 807–813.
- (12) Yin, Q.; Tan, J. M.; Besson, C.; Geletii, Y. V.; Musaev, D. G.; Kuznetsov, A. E.; Luo, Z.; Hardcastle, K. I.; Hill, C. L. *Science* **2010**, *328*, 343–345.
- (13) Wasylenko, D. J.; Ganesamoorthy, C.; Borau-Garcia, J.; Berlinguette, C. P. *Chem. Commun.* **2011**, *47*, 4249–4251.
- (14) Barnett, S. M.; Goldberg, K. I.; Mayer, J. M. *Nat. Chem.* **2012**, *4*, 498–502.
- (15) Zhang, M.-T.; Chen, Z.; Kang, P.; Meyer, T. J. *J. Am. Chem. Soc.* **2013**, *135*, 2048–2051.
- (16) Blakemore, J. D.; Schley, N. D.; Balcells, D.; Hull, J. F.; Olack, G. W.; Incarvito, C. D.; Eisenstein, O.; Brudvig, G. W.; Crabtree, R. H. *J. Am. Chem. Soc.* **2010**, *132*, 16017–16029.
- (17) Becke, A. D. *J. Chem. Phys.* **1993**, *98*, 5648–5652.
- (18) Andrae, D.; Häußermann, U.; Dolg, M.; Stoll, H.; Preuß, H. *Theor. Chim. Acta* **1990**, *77*, 123–141.
- (19) Kazaryan, A.; Baerends, E. J. *J. Comput. Chem.* **2013**, *34*, 870–878.
- (20) Weigend, F.; Ahlrichs, R. *Phys. Chem. Chem. Phys.* **2005**, *7*, 3297–3305.
- (21) Raghavachari, K.; Trucks, G. W.; Pople, J. A.; Head-Gordon, M. *Chem. Phys. Lett.* **1989**, *157*, 479–483.
- (22) Vilella, L.; Vidossich, P.; Balcells, D.; Lledós, A. *Dalton Trans.* **2011**, *40*, 11241–11247.
- (23) Wang, C.; Wang, J.-L.; Lin, W. *J. Am. Chem. Soc.* **2012**, *134*, 19895–19908.
- (24) Grotjahn, D. B.; Brown, D. B.; Martin, J. K.; Marelius, D. C.; Abadjian, M.-C.; Tran, H. N.; Kalyuzhny, G.; Vecchio, K. S.; Specht, Z. G.; Cortes-Llamas, S. A.; Miranda-Soto, V.; van Niekerk, C.; Moore, C. E.; Rheingold, A. L. *J. Am. Chem. Soc.* **2011**, *133*, 19024–19027.
- (25) Frisch, M. J.; Trucks, G. W.; Schlegel, H. B.; Scuseria, G. E.; Robb, M. A.; Cheeseman, J. R.; Scalmani, G.; Barone, V.; Mennucci, B.; Petersson, G. A.; Nakatsuji, H.; Caricato, M.; Li, X.; Hratchian, H. P.; Izmaylov, A. F.; Bloino, J.; Zheng, G.; Sonnenberg, J. L.; Hada, M.; Ehara, M.; Toyota, K.; Fukuda, R.; Hasegawa, J.; Ishida, M.; Nakajima, T.; Honda, Y.; Kitao, O.; Nakai, H.; Vreven, T.; Montgomery, J. A., Jr.

Peralta, J. E.; Ogliaro, F.; Bearpark, M.; Heyd, J. J.; Brothers, E.; Kudin, K. N.; Staroverov, V. N.; Kobayashi, R.; Normand, J.; Raghavachari, K.; Rendell, A.; Burant, J. C.; Iyengar, S. S.; Tomasi, J.; Cossi, M.; Rega, N.; Millam, M. J.; Klene, M.; Knox, J. E.; Cross, J. B.; Bakken, V.; Adamo, C.; Jaramillo, J.; Gomperts, R.; Stratmann, R. E.; Yazyev, O.; Austin, A. J.; Cammi, R.; Pomelli, C.; Ochterski, J. W.; Martin, R. L.; Morokuma, K.; Zakrzewski, V. G.; Voth, G. A.; Salvador, P.; Dannenberg, J. J.; Dapprich, S.; Daniels, A. D.; Farkas, Ö.; Foresman, J. B.; Ortiz, J. V.; Cioslowski, J.; Fox, D. J. *Gaussian 09*, revision D.01; Gaussian, Inc.: Wallingford CT, 2009.

(26) Marenich, A. V.; Cramer, C. J.; Truhlar, D. G. *J. Phys. Chem. B* **2009**, *113*, 6378–6396.

(27) Reiher, M.; Salomon, O.; Hess, B. A. *Theor. Chem. Acc.* **2001**, *107*, 48–55.

(28) Grimme, S.; Antony, J.; Ehrlich, S.; Krieg, H. *J. Chem. Phys.* **2010**, *132*, 154104.

(29) Zhao, Y.; Truhlar, D. G. *Theor. Chem. Acc.* **2008**, *120*, 215–241.

(30) Zhao, Y.; Truhlar, D. G. *J. Chem. Phys.* **2006**, *125*, 194101.

(31) Adamo, C.; Barone, V. *J. Chem. Phys.* **1999**, *110*, 6158–6170.

(32) Camaioni, D. M.; Schwerdtfeger, C. A. *J. Phys. Chem. A* **2005**, *109*, 10795–10797.

(33) Siegbahn, P. E. M. *Chem.—Eur. J.* **2008**, *14*, 8290–8302.

(34) Siegbahn, P. E. M. *Acc. Chem. Res.* **2009**, *42*, 1871–1880.

(35) Blomberg, M. R. A.; Siegbahn, P. E. M. *Biochim. Biophys. Acta* **2010**, *1797*, 129–142.

(36) Siegbahn, P. E. M.; Blomberg, M. R. A. *Chem. Rev.* **2010**, *110*, 7040–7061.

(37) Li, X.; Chen, G.; Schinzel, S.; Siegbahn, P. E. M. *Dalton. Trans.* **2011**, *40*, 11296–11307.

(38) Siegbahn, P. E. M. *J. Photochem. Photobiol., B* **2011**, *104*, 94–99.

(39) Siegbahn, P. E. M. *Phys. Chem. Chem. Phys.* **2012**, *14*, 4849–4856.

(40) Li, X.; Siegbahn, P. E. M. *J. Am. Chem. Soc.* **2013**, *135*, 13804–13813.

(41) Liao, R. Z.; Li, X.; Siegbahn, P. E. M. *Eur. J. Inorg. Chem.* **2014**, 728–741.

(42) Isse, A. A.; Gennaro, A. *J. Phys. Chem. B* **2010**, *114*, 7894–7899.

(43) Marenich, A. V.; Ho, J.; Coote, M.; Cramer, C. J.; Truhlar, D. G. *Phys. Chem. Chem. Phys.* **2014**, *16*, 15068–15106.

(44) Marenich, A. V.; Majumdar, A.; Lenz, M.; Cramer, C. J.; Truhlar, D. G. *Angew. Chem., Int. Ed.* **2012**, *51*, 12810–12814.

(45) *CRC Handbook of Chemistry and Physics*, 93rd ed.; Haynes, W. M., Ed.; CRC Press: Boca Raton, FL, 2013.

(46) Venturini, A.; Barbieri, A.; Reek, J. N. H.; Hettterscheid, D. G. H. *Chem.—Eur. J.* **2014**, *20*, 5358–5368.